

Cite this: *Nanoscale*, 2019, **11**, 13832

Control of upconversion luminescence by gold nanoparticle size: from quenching to enhancement†

Diego Mendez-Gonzalez, ^a Sonia Melle, ^{*b} Oscar G. Calderón, ^b
 Marco Laurenti, ^a E. Cabrera-Granado, ^b Ana Egatz-Gómez, ^{c,d}
 Enrique López-Cabarcos, ^a Jorge Rubio-Retama ^a and Elena Díaz ^e

Metallic nanostructures have the potential to modify the anti-Stokes emission of upconverting nanoparticles (UCNPs) by coupling their plasmon resonance with either the excitation or the emission wavelength of the UCNPs. In this regard gold nanoparticles (AuNPs) have often been used in sensors for UCNP luminescence quenching or enhancement, although systematic studies are still needed in order to design optimal UCNP–AuNP based biosensors. Amidst mixed experimental evidence of quenching or enhancement, two key factors arise: the nanoparticle distance and nanoparticle size. In this work, we synthesize AuNPs of different sizes to assess their influence on the luminescence of UCNPs. We find that strong luminescence quenching due to resonance energy transfer is preferentially achieved for small AuNPs, peaking at an optimal size. A further increase in the AuNP size is accompanied by a reduction of luminescence quenching due to an incipient plasmonic enhancement effect. This enhancement counterbalances the luminescence quenching effect at the biggest tested AuNP size. The experimental findings are theoretically validated by studying the decay rate of the UCNP emitters near a gold nanoparticle using both a classical phenomenological model and the finite-difference time-domain method. Results from this study establish general guidelines to consider when designing sensors based on UCNPs–AuNPs as donor–quencher pairs, and suggest the potential of plasmon-induced luminescence enhancement as a sensing strategy.

Received 8th March 2019,

Accepted 2nd July 2019

DOI: 10.1039/c9nr02039j

rsc.li/nanoscale

1. Introduction

Over the last few years, lanthanide doped upconverting nanoparticles (UCNPs) have emerged as promising materials due to their capacity to exhibit photon upconversion.^{1–4} UCNPs are able to absorb low-energy photons in the infrared or near infrared (NIR) range and emit high-energy photons in the UV-Vis range. This process can take place through different

mechanisms, with energy-transfer upconversion (ETU) and excited-state absorption (ESA) being by far the most common.^{5–7} These mechanisms involve multistep absorption of two or more photons by an intermediate meta-stable state which promotes the population of a higher excited state from which upconversion emission occurs.⁸ This gives rise to high conversion efficiency with no need for intense coherent excitation or ultra-fast laser sources, which are required for other nonlinear multiphoton processes. In addition, the large anti-Stokes shifts, and the lack of photo-bleaching and blinking provide special features to these nanoparticles which make them ideal candidates to create sensors and bioassays powered by UCNPs.^{9,10} Many of these sensors exploit the so-called resonance energy transfer (RET) as the action mechanism to detect a specific target molecule.^{11,12} This is normally based on the energy transfer from the excited state of a UCNP (donor) to the ground state of a molecule or other material which acts as an acceptor, resulting in a variation of the UCNP luminescence.¹³

Plasmonic nanostructures placed in close proximity to UCNPs have been demonstrated to be an excellent tool for tuning the upconversion luminescence by enhancing or quenching the luminescence intensity.¹⁴ Signal enhancement

^aDepartment of Chemistry in Pharmaceutical Sciences, Complutense University of Madrid, E-28040 Madrid, Spain

^bDepartment of Optics, Complutense University of Madrid, E-28037 Madrid, Spain. E-mail: smelle@fis.ucm.es

^cSchool of Molecular Sciences, Arizona State University, Tempe, Arizona 85287, USA

^dCenter for Applied Structural Discovery, The Biodesign Institute, Arizona State University, Tempe, Arizona 85287, USA

^eGISC, Department of Materials Physics, Complutense University of Madrid, E-28040 Madrid, Spain

† Electronic supplementary information (ESI) available: Analysis of the luminescence decay signals; luminescence rise signals and absorbance spectra for dispersions containing 66 nm-diameter AuNPs and APTES- and non-APTES-functionalized UCNPs; description of the parameters used to simulate luminescence decay curves from UCNPs interacting with AuNPs. See DOI: 10.1039/C9NR02039J

is usually achieved by matching the metallic nanostructure surface plasmon resonance (SPR) wavelength with the excitation wavelength of the UCNP, typically ~ 980 nm. This leads to an increased excitation rate due to a local field enhancement near the metal nanostructure. Luminescence enhancement can also be achieved by increasing the radiative decay rate of the emitters (Purcell effect). This happens when the SPR wavelength of the metallic nanostructure matches the emission wavelength of the UCNPs. In addition to luminescence enhancement, when the latter condition is fulfilled, a short-range effect may arise through non-radiative RET from the emitter ion to the metal nanostructure, namely, the quenching of luminescence.

Most experimental evidence has revealed that the luminescence of UCNPs can be enhanced by interactions with several types of plasmonic metallic nanostructures such as silver nanogratings,¹⁵ gold pyramid arrays,¹⁶ gold nanohole arrays,¹⁷ disk-coupled dots-on-pillar antenna arrays,¹⁸ metal-insulator-metal nanostructures,¹⁹ gold nanorods,²⁰ and gold nanotriangles.²¹ In addition, there are a few examples of studies on the transition from luminescence quenching to enhancement by changing the distance between the upconverting emitter and the metallic nanostructure.^{22–26}

Due to its feasibility, spherical metal nanoparticles (NPs) are commonly used to engineer nanomaterials with novel metallic, electronic and optical properties. Within the context of tuning the UCNP luminescence, it is worth noting that metal NPs (typically Ag and Au) exhibit plasmon absorption in the 400–600 nm range, far away from the excitation wavelength of UCNPs. Thus, in principle, one would expect that this would limit the effect of metal NPs on UCNP excitation enhancement. However, different effects of metal NPs on upconversion luminescence have been found. Schietinger *et al.* found plasmon enhanced luminescence in a single 30 nm diameter UCNP coupled to a AuNP of similar or larger size (60 nm).²⁷ There, a reduction of the upconversion luminescence rise and decay times was observed, an indication that both the excitation and emission processes are affected by the plasmon resonance of the AuNP. The luminescence of 180 nm diameter UCNPs has been also enhanced by Au nano-seed coatings.²⁸ In this case, the authors attributed the effect to an increase of the emission rate by surface plasmon-coupled emission. Note that this coupling occurs when the upconversion emission band overlaps the plasmonic resonance. On the other hand, luminescence quenching was found in other studies. For example, Zhang *et al.*²⁹ reported luminescence quenching in a dispersion of 120 nm diameter UCNPs with a 20 nm-thick silica shell interacting with 9.4 nm-diameter AuNPs. Luminescence quenching induced by non-radiative RET was also demonstrated in UCNPs interacting with AuNPs of similar or smaller sizes.^{30,31} In fact, non-radiative energy transfer between UCNPs and AuNPs has been proposed for melamine detection³⁰ and emitter–quencher-based bioassays.³¹

Amidst the wide variety of experimental evidence regarding the control of upconversion luminescence by surface plasmon

nanostructures, two key ingredients for the particular properties of the hybrid systems arise: the size of the subsystems and the distance between them. Indeed, these two are not completely independent factors. As a single UCNP contains multiple Er^{3+} emitter ions distributed throughout, the extent of the effects experienced by each emitter due to its proximity to a AuNP is conditioned by the relative sizes of the AuNP and the UCNP. This work points out the crucial importance of the size of the metal NPs in the plasmon-controlled luminescence. We study the luminescence of UCNPs interacting with AuNPs from well below to above the size of the UCNP. In addition, we develop an in-depth theoretical study that highlights the relevance of the donor ion distribution inside the UCNP in order to explain our experimental findings. This analysis is performed from two different perspectives where the distances between the individual ion donors and the metallic NP are explicitly considered. Our primary goal is to characterize from a fundamental point of view the competition between different plasmon-induced mechanisms as the size of the AuNP increases. This reveals optimum AuNP sizes to design luminescence quenching- or enhancement-based nanosensors.

2. Experimental section

2.1. Chemicals

Gold(III) chloride hydrate 99.995%, sodium citrate tribasic dehydrate $\geq 99.0\%$, polyvinylpyrrolidone (PVP) 40k, $\text{YCl}_3 \cdot 6\text{H}_2\text{O}$ 99.99%, $\text{YbCl}_3 \cdot 6\text{H}_2\text{O}$ 99.998%, $\text{ErCl}_3 \cdot 6\text{H}_2\text{O}$ 99.9%, 1-octadecene (1-ODE) technical grade 90%, oleic acid (OA) technical grade 90%, NH_4F 98%, NaOH 98%, methanol 99.9%, *n*-hexane 97%, tetraethyl orthosilicate 98%, NH_4OH ACS reagent 28–30%, IGEPAL CO-520 and (3-aminopropyl)-triethoxysilane (APTES) 99% were acquired from Sigma-Aldrich. Absolute ethanol 99.5% was purchased from PanReac AppliChem. All chemicals were used as received without further purification.

2.2. Synthesis of AuNPs

$\text{Au}_{4 \text{ nm}}$ was obtained using the following procedure.³² 480 μL of 5 mM HAuCl_4 were mixed with 1.68 mL of deionized water and 2 mL of PVP40K (7 mg mL^{-1}) for 10 minutes. 200 μL of freshly prepared 0.1 M NaBH_4 were added dropwise under vigorous magnetic stirring and the solution rapidly changed from colorless to a deep brownish color. Prior to use, the synthesized nanoparticles were aged until the UV-Vis spectrum remained unchanged and the color of the solution was brownish-red. The AuNPs were used in further experiments without washing.

The synthesis of $\text{Au}_{14 \text{ nm}}$ was carried out using the following protocol.³³ In a 250 mL two-necked round bottom flask 99.2 mL of H_2O and 0.8 mL of 25 mM HAuCl_4 were mixed, and the resulting solution was boiled. At this point, 1 mL of trisodium citrate (3 mM) was added and the solution rapidly turned colorless. After 5 minutes the solution color changed to black-blue, and finally after 5 minutes to deep red. The solution was kept at this temperature for 10 more minutes, cooled

down to room temperature (RT), and stored for further experiments.

The synthesis of AuNPs with bigger sizes (Au_{21 nm} to Au_{66 nm}) was carried out following a step-by-step seed-mediated growth process described by Bastús *et al.*³⁴ First, gold seeds were synthesized by adding 1 mL of HAuCl₄ (25 mM) into a round-bottom flask connected to a Liebig condenser, containing 150 mL sodium citrate (2.2 mM) at 100 °C under stirring. The reaction was allowed to proceed until a red-wine color was obtained. Then the solution was cooled to 90 °C, 1 mL of HAuCl₄ (25 mM) was added, and the growth reaction ran for 30 min. This step was repeated again to yield Au_{21 nm}. Next, a 55 mL Au_{21 nm} aliquot was extracted and stored, and 53 mL Milli-Q water and 2 mL sodium citrate (60 mM) were added to the flask in order to prepare the repetition of a new growth round over Au_{21 nm}. After two consecutive growth rounds, each consisting of three steps of 1 mL HAuCl₄ addition/30 min reaction time (90 °C), a later extraction of 55 mL of the product and a final addition of 53 mL Milli-Q water and 2 mL sodium citrate (60 mM), Au_{36 nm} was obtained. One, two and four additional growth rounds were required to obtain Au_{41 nm}, Au_{52 nm}, and Au_{66 nm}, respectively.

2.3. Synthesis of UCNPs

NaY_{0.78}F₄:Yb_{0.2},Er_{0.02} UCNPs were synthesized using the thermal coprecipitation method.³⁵ In a three-necked round-bottom flask were placed 236 mg of YCl₃, 78 mg of YbCl₃, and 7.8 mg of ErCl₃ with 15 mL of 1-octadecene and 6 mL of oleic acid. The solution was heated at 140 °C until all solid was dissolved under a nitrogen atmosphere. Then, the solution was cooled to RT and a 10 mL methanol solution with 110 mg of NaOH and 157 mg of NH₄F was added dropwise under vigorous magnetic stirring over 15 minutes. The mixture was stirred for 15 minutes, then heated at 80 °C for 15 minutes under a nitrogen flow, and finally kept under vacuum for 15 minutes at 80 °C to ensure the removal of water/methanol traces. The flask was placed in a heating mantle and heated at 320 °C for 45 minutes under a nitrogen atmosphere. Finally, the solution was cooled to RT, the solution was split into 4 tubes and a solution of methanol–water with a ratio of 2 : 1 was added. The solution was centrifuged at 8500 rpm for 10 minutes, the supernatant discarded, the pellet was resuspended in a small aliquot of *n*-hexane, and the process was repeated two additional times. The pellet was dispersed in *n*-hexane and used in the next step.

The above synthesized NaY_{0.78}F₄:Yb_{0.2},Er_{0.02} UCNPs were covered with a thin layer of silica using the following method.³⁶ Briefly, 240 mg of IGEPAL CO-520 was mixed with 4.2 mL of *n*-hexane, 0.8 mL of the UCNPs (20 mg mL⁻¹), and 40 μL of NH₃ at 29%. The suspension was sonicated until a clear and colorless solution was obtained. Finally, 20 μL of TEOS was added to the solution and stirred for 1 day at RT. The core–shell UCNPs@SiO₂ were centrifuged at 8500 rpm for 10 minutes, the supernatant was discarded and the solid was resuspended with absolute ethanol and centrifuged two additional times. These core–shell UCNPs@SiO₂ were stored

in absolute ethanol at a concentration of 4 mg mL⁻¹ and used as a reference (non-APTES-UCNPs). Finally, we dispersed core–shell UCNPs@SiO₂ in 5 mL of absolute ethanol and 30 μL of APTES was added to the solution and stirred for 1 day at RT. The modified core–shell UCNPs@SiO₂-NH₂ were centrifuged at 8500 rpm for 10 minutes, the supernatant was discarded and the solid was resuspended with absolute ethanol and centrifuged two additional times. The core–shell UCNPs@SiO₂-NH₂ were stored in absolute ethanol at a concentration of 4 mg mL⁻¹ and used for further experiments (APTES-UCNPs).

2.4. Morphological characterization

Electron microscopy images were acquired in transmission mode (TEM) using a JEM 1010 microscope (JEOL, Japan) working at 80 kV and equipped with a Gatan (USA) digital camera (model 782).

2.5. Optical characterization

Absorbance spectra of AuNP aqueous dispersions at different concentrations were measured with a Varian Cary 300 Bio UV-Vis spectrophotometer with 10 mm path length cuvettes.

The emission of the UCNPs was measured with an upconversion fluorescence home-built system. The excitation laser beam comes from a pigtailed 10 W CW laser (JDSU, L4-9897603) operating at 976 nm and provided with a current and temperature controller (ILX Lightwave, LDX-36025-12 and LDT-5525B, respectively). The laser beam is transmitted through a long-pass dichroic filter (Semrock, FF757-Di01), and then focused on the sample with a 10× objective. The upconversion luminescence coming from the sample is reflected by the dichroic mirror towards a short-pass filter, which blocks the IR reflected radiation (Semrock, FF01-775/SP). Then, the beam is focused into an optical fiber connected to a monochromator (Horiba Jobin Yvon, iHR320). The monochromator is equipped with a photomultiplier tube (Hamamatsu, R928) and uses a 1800 gr per mm grating blazed at 500 nm. In order to characterize the laser intensity at the sample, we measured the laser power with a thermal sensor power meter (Thorlabs, S310C) and the beam size (FWHM) using the slit scan technique,³⁷ the size being around 300 μm. In our measurements, we used an excitation laser current of 2 A, which corresponds to a laser power close to 1 W at the sample position. Then, the laser intensity on the sample was around 1.4 kW cm⁻². This allows us to ensure that the laser operates below the excitation saturation intensity of the transition ²F_{7/2} → ²F_{5/2} of the Yb³⁺ ions, which is $I_{\text{sat}} = \hbar\omega / (2\sigma^Y \tau^Y) = 3 \text{ kW cm}^{-2}$, where $\tau^Y = 2 \text{ ms}$ is the excited level lifetime, $\sigma^Y = 1.7 \times 10^{-20} \text{ cm}^2$ is the absorption cross-section, and $\hbar\omega$ the transition energy (resonant with an excitation laser wavelength at 976 nm).

Upconversion luminescence spectra of APTES-UCNPs and non-APTES-UCNPs, and their combination with the different AuNPs were measured as follows: three consecutive spectra were collected at 2-minute intervals. Then, we computed the average intensity of the integrated area of the spectra within the green emission band, and we took the maximum deviation

as the error. Results presented without error bars correspond to a single representative measurement.

Luminescence lifetimes were measured using the time-resolved photon counting method. The laser current controller allows generating light excitation pulses of 40 μ s with a repetition rate of 125 Hz. The luminescence emission at 540 nm is detected by the photomultiplier tube, which is directly connected (without using a pre-amplifier) to a 50 Ω input of a digital oscilloscope (Agilent, DSO9104A). A signal from the laser current controller is used to trigger the oscilloscope. We developed a Matlab program which analyzes directly in the oscilloscope each recorded signal in real-time. This code simulates the discriminator and the multichannel counter.³⁸ Upon analysis of more than 5000 trigger signals, we obtain a luminescence decay curve. The luminescence decay time was obtained by fitting the decay curve to a single exponential function (see ESI† section S1 for details).

3. Results and discussion

In order to study the effect of the AuNP size on the upconversion luminescence, we synthesized AuNPs with diameters ranging from 3.9 nm to 66 nm. Absorbance spectra for aqueous dispersions of the synthesized AuNPs with different sizes are shown in Fig. 1A. For 3.9 nm-diameter AuNPs the presence of a shoulder located around 500–520 nm indicates the incipient appearance of the localized surface plasmon.^{39–41} As the AuNP diameter increases, the localized surface plasmon resonance is slightly red-shifted. For each AuNP size, the nanoparticle concentration in the aqueous dispersion used in the

Table 1 Characteristics of the AuNP dispersions used in the experiments

Name of AuNPs	Diameter $2a^a$ (nm)	Concentration ^b (NPs/mL)	Zeta potential (mV)
Au ₄ nm	3.9 ± 0.8	1.58×10^{14}	-28.3 ± 0.8
Au ₁₄ nm	14 ± 2	1.66×10^{12}	-42 ± 4
Au ₂₁ nm	21 ± 3	1.24×10^{12}	-38.7 ± 0.8
Au ₃₆ nm	36 ± 4	5.14×10^{11}	-32.5 ± 0.9
Au ₄₁ nm	41 ± 4	4.1×10^{11}	-31 ± 3
Au ₅₂ nm	52 ± 5	2.14×10^{11}	-34.1 ± 0.5
Au ₆₆ nm	66 ± 9	1.09×10^{11}	-32 ± 2

^a From TEM images. ^b From absorbance at 400 nm.

experiments is roughly determined by measuring the absorbance at 400 nm.⁴² Results are presented in Table 1.

To prepare the UCNPs@SiO₂, first we produced mono-disperse UCNPs of NaYF₄:Yb,Er and oleic acid as a capping agent. TEM images show highly monodisperse UCNPs with an average diameter of 18 ± 2 nm (Fig. 2A). The hydrophobic UCNPs were covered with a thin silica shell using a reverse-microemulsion method,³⁶ which made them hydrophilic. A silica shell thickness of 3.8 ± 0.5 nm was determined from TEM images (Fig. 2B). The upconversion luminescence emission spectrum of core-shell UCNPs@SiO₂ under a 976 nm CW excitation laser is shown in Fig. 1A (gray curve, right axis). Two green emission peaks near 525 nm and 540 nm are observed which correspond to the $^2H_{11/2} \rightarrow ^4I_{15/2}$ and $^4S_{3/2} \rightarrow ^4I_{15/2}$ transitions of the Er³⁺ ions, respectively. Fig. 1A demonstrates very good overlap between these green emission bands and the localized surface plasmon resonance wavelength of the AuNPs. The energy level scheme of the system, including the upconversion process by means of energy transfer from Yb³⁺ ions to Er³⁺ ions and the interaction with the AuNPs, is shown in Fig. 1B.

After separately characterizing each of the nanoparticle components for our hybrid system of interest, we prepared UCNPs with amine-group functionalized silica shells (UCNPs@SiO₂-NH₂). The amine groups on the UCNPs@SiO₂ directly bind to the AuNP surface by interacting with the AuNP original ligands (citrate or PVP), yielding AuNP-decorated UCNPs. Amines have lone electron pairs which can also coordinate to the surface of the AuNPs. At pH below 10, primary amines exist predominantly as positively charged R-NH₃⁺ groups. In our case, the pH range of the colloidal solution resulting from the mixing of the AuNPs and the UCNPs@SiO₂-NH₂ was 6.5–7. Consequently, the interaction between the positively charged UCNPs@SiO₂-NH₂ (zeta potential = 33.3 ± 0.3 mV) and the negatively charged AuNPs (see the zeta potential values in Table 1) is preferentially electrostatic, rather than coordinative. Fig. 2C, D and E show highly monodisperse UCNPs@SiO₂-NH₂ decorated with AuNPs of different sizes (Au₄ nm, Au₂₁ nm, and Au₆₆ nm, respectively).

In order to determine the volumes of the different AuNP dispersions suitable for influencing the green luminescence of UCNPs, spectral measurements were taken after addition of an

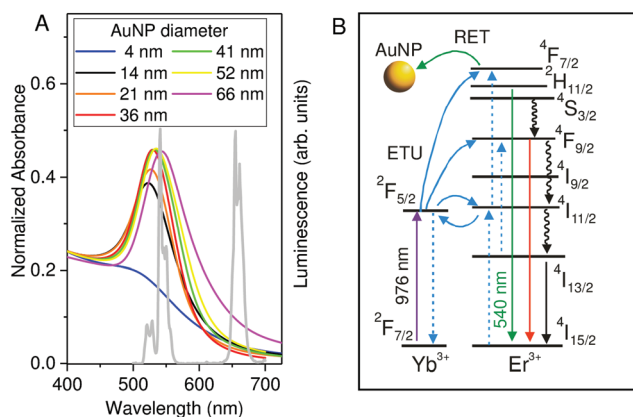


Fig. 1 (A) (Left axis) Absorbance spectra of aqueous dispersions of AuNPs with different sizes. All curves were normalized to the absorbance at 400 nm. (Right axis, gray curve) Luminescence spectrum for the UCNPs ethanol dispersion when excited at 976 nm. (B) Energy level diagram for Yb³⁺ and Er³⁺ ions. Blue lines represent the ETU mechanism which populates the green emission levels $^2H_{11/2}$ and $^4S_{3/2}$ with a 976 nm laser. The luminescence emission from these levels is represented by a solid green line. Solid lines represent the radiative decays while wavy lines are the non-radiative decays to the next lower level. The RET process from the green levels to the AuNP is also shown.

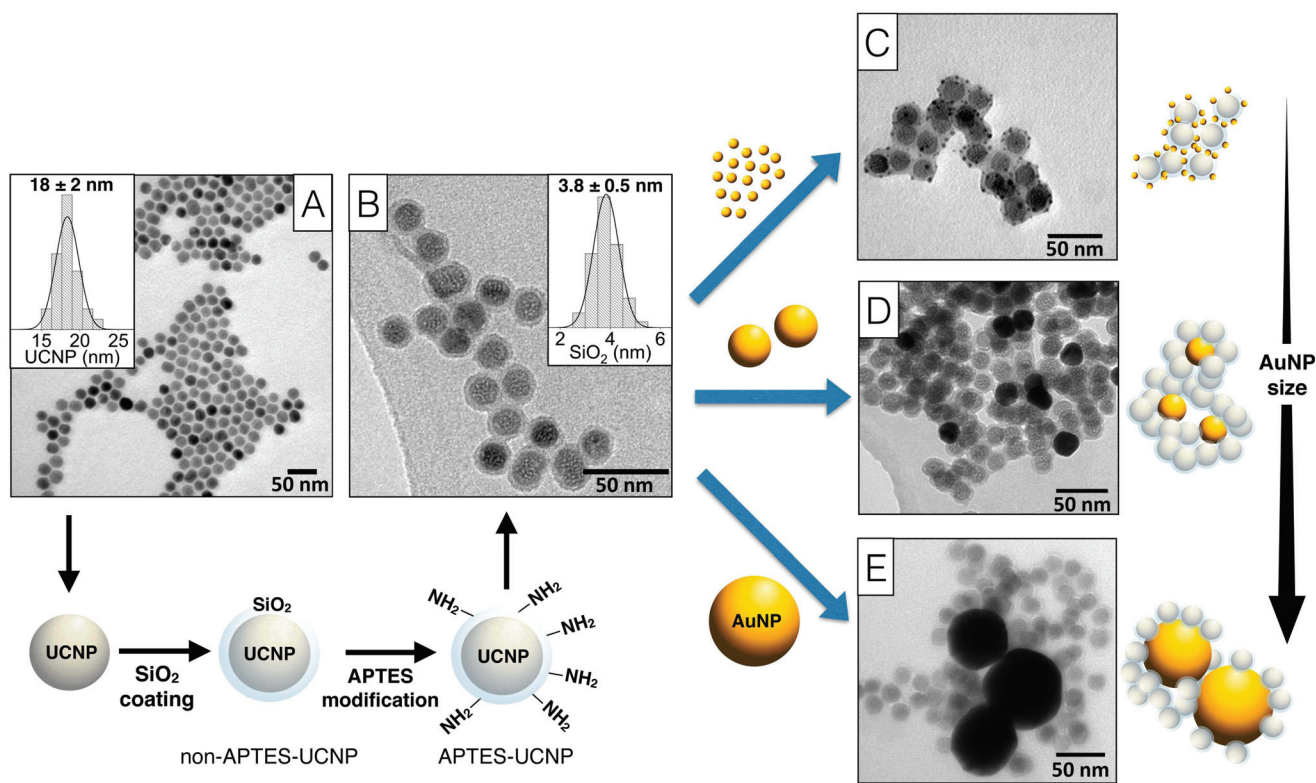


Fig. 2 (A) TEM image of NaYF₄:Yb,Er UCNPs, with the inset showing a particle diameter histogram, (B) TEM image of NaYF₄:Yb,Er@SiO₂-NH₂ UCNPs, with the inset showing a silica shell thickness histogram, and (C–E) TEM images of NaYF₄:Yb,Er@SiO₂-NH₂ UCNPs after attaching (C) Au_{4 nm}, (D) Au_{21 nm}, and (E) Au_{66 nm} NPs.

increasing volume of the AuNP aqueous dispersion to a fixed volume of the UCNP ethanol dispersion, until no further modification of the luminescence intensity was observed. We mixed 100 μL of an ethanol dispersion of UCNP@SiO₂-NH₂ (APTES-UCNPs) at 0.1 g L⁻¹ (6.4 $\times 10^{-9}$ M) in a 3 mm length cuvette with an increasing volume of the AuNP aqueous dispersion. Because the interaction between UCNPs and AuNPs occurs when APTES is present in the system, we used another ethanol dispersion containing UCNP@SiO₂ (non-APTES-UCNPs) as a reference. The reference samples were prepared in exactly the same way, *i.e.*, 100 μL of UCNP@SiO₂ in ethanol at 0.1 g L⁻¹ mixed with an increasing volume of the AuNP dispersion. This reference was used as a control to isolate the effects arising from the interaction between UCNPs and AuNPs, since in both samples all conditions, characteristics, volumes and concentrations of the NPs are the same, but the direct interaction between them is only promoted when APTES is present. A comparison of the luminescence spectra of both samples (APTES-UCNPs and non-APTES-UCNPs) in the presence of AuNPs allows the optical response due to the specific UCNP@SiO₂-NH₂/AuNP interaction to be clearly distinguished.

First, we focus on AuNPs with a size similar to or smaller than the UCNPs. Let us analyze in detail the case corresponding to Au_{21 nm} NPs. Fig. 3A shows the upconversion luminescence spectra for the APTES-UCNP and non-

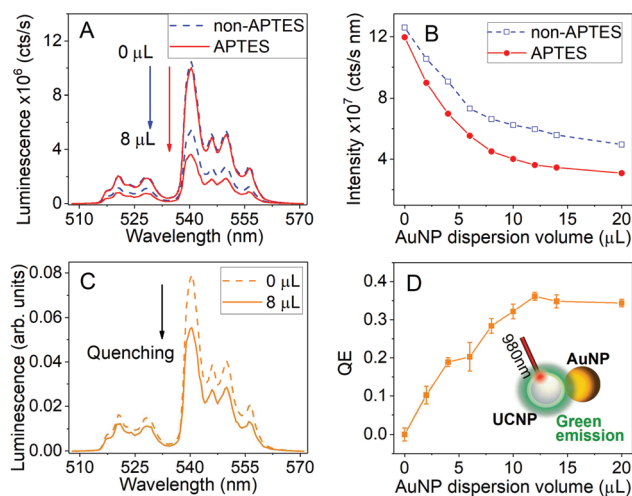


Fig. 3 (A) Luminescence spectra for 100 μL dispersions of APTES-UCNPs (red solid line), and non-APTES-UCNPs (blue dashed line), before and after the addition of 8 μL of Au_{21 nm}. (B) Intensity (integrated luminescence spectrum) as a function of the AuNP dispersion volume added to APTES and non-APTES UCNPs. (C) Luminescence spectra for the APTES-UCNPs normalized to the corresponding spectra for the non-APTES-UCNPs for added volumes of the Au_{21 nm} dispersion. (D) Luminescence quenching efficiency, QE, as a function of the volume of the Au_{21 nm} dispersion added to the UCNPs.

APTES-UCNP dispersions. The luminescence intensities of both samples are the same before adding the AuNPs and globally decrease when a volume of 8 μL of the Au_{21 nm} dispersion is added. However, a stronger luminescence decrease occurs for the APTES-UCNPs. This can be attributed to the attachment of the AuNPs to the APTES-UCNPs and the luminescence energy transfer between them, which leads to luminescence quenching. This behavior remains for additional volumes of the AuNP dispersion, as shown in Fig. 3B. In order to quantify this plasmon-induced luminescence quenching, we normalized the spectra of the APTES-UCNPs with the integrated spectra of the non-APTES-UCNPs for the same AuNP added volume (see Fig. 3C). This allows us to identify the effects induced by plasmon-interactions, since other effects, such as solvent-induced luminescence quenching, are removed. Finally, we calculate the quenching efficiency, QE, as the relative change of the luminescence intensity as follows:

$$QE = 1 - \frac{I_A}{I_{NA}}, \quad (1)$$

where I_A and I_{NA} are the upconversion luminescence intensities for the APTES-UCNP and non-APTES-UCNP samples, respectively. Fig. 3D shows the QE as a function of the volume of the AuNP dispersion added to 100 μL UCNP ethanol dispersion. Initially, when small volumes are added, the QE increases until it reaches a plateau where $QE \sim 35\%$ and the ratio of intensities $I_A/I_{NA} \approx 0.65$. A qualitative similar behavior was found for smaller AuNPs (Au_{4 nm} and Au_{14 nm}), and even for a little larger AuNPs (Au_{36 nm}). However, if the AuNP size is much larger than the size of the UCNPs, the behavior of the upconversion luminescence turns out to be rather different as shown below.

Fig. 4A shows the upconversion luminescence spectra for the APTES-UCNP and the non-APTES-UCNP dispersions. In both cases, a global decrease of luminescence takes place when we add a volume of 8 μL of the Au_{66 nm} dispersion, as observed in the case of Au_{21 nm}. However, in this case, quenching is reduced when the AuNPs are attached to the APTES-UCNPs. This seems to indicate that a plasmon-induced phenomenon, directly related to the interaction between the AuNPs and the UCNPs, leads, for this particular AuNP size, to luminescence enhancement. Indeed, when increasing the volume of the AuNP dispersion, this behavior is reproduced, as can be seen in Fig. 4B. Although most of the previous studies on plasmon-enhanced luminescence of UCNPs are based on excitation enhancement, in our case, this mechanism is not expected to occur, since the excitation wavelength is far away from the AuNP plasmon resonance. Still, we performed two additional tests in this regard. Fig. S2† analyzes the luminescence rise time for both APTES-UCNPs and non-APTES-UCNPs with Au_{66 nm} NPs. Our results confirm that both samples follow the same temporal behavior, which corroborates the absence of plasmon-induced excitation enhancement in our experiments. Fig. S3† shows the absorbance spectra of these two UCNP-Au_{66 nm} NP samples, which reveal

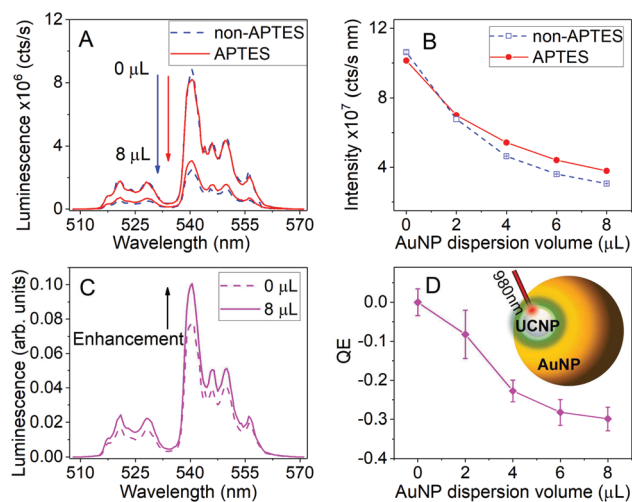


Fig. 4 (A) Luminescence spectra for 100 μL dispersions of APTES-UCNPs (red solid line), and non-APTES UCNP (blue dashed line) dispersions, before and after the addition of 8 μL of Au_{66 nm}. (B) Intensity (integrated luminescence spectrum) as a function of the AuNP dispersion volume added to APTES and non-APTES UCNPs. (C) Luminescence spectra for the APTES-UCNPs normalized to the corresponding spectra for the non-APTES-UCNPs for added volumes of the Au_{66 nm} dispersion. (D) Luminescence quenching efficiency, QE, as a function of the volume of the Au_{66 nm} dispersion added to the UCNPs.

that the UCNP–AuNP interactions mediated by APTES do not affect the plasmon resonance.

Once again, in order to clearly identify the luminescence enhancement due to the interaction of UCNPs with AuNPs, we normalized the spectra of the APTES-UCNPs with the integrated spectra for the non-APTES-UCNPs with the same added volume of AuNPs (see Fig. 4C). Finally, we calculated the quenching efficiency as a function of the added volume of the Au_{66 nm} dispersion (see Fig. 4D). In this case, a negative value of QE is achieved, which actually characterizes enhancement efficiency. After an initial growth, the QE roughly reaches a plateau where $QE \sim -30\%$ and, thus, the associated enhancement factor is $I_A/I_{NA} \approx 1.25$. In view of these results, we conclude that for large enough AuNPs, although the RET phenomenon is expected, it seems that another plasmon-induced luminescence enhancement phenomenon is dominant.

Last, in order to get information about the competing effects within samples with different AuNP sizes, we plot QE as a function of the ratio between the total masses of AuNPs and UCNPs present in the sample under characterization. This allows us to directly identify the dominant effect as a function of AuNP-size, while keeping the same Au mass in the sample. Results collected in Fig. 5 indicate that the interaction of the small AuNPs with the UCNPs gives rise to luminescence quenching, whereas the interaction of the large AuNPs produces the opposite effect, namely, luminescence enhancement. As mentioned before, these results show clear features of the existence of two competing effects governing the optical response of the system. The interplay between these two plasmon-induced phenomena leads to a transition from

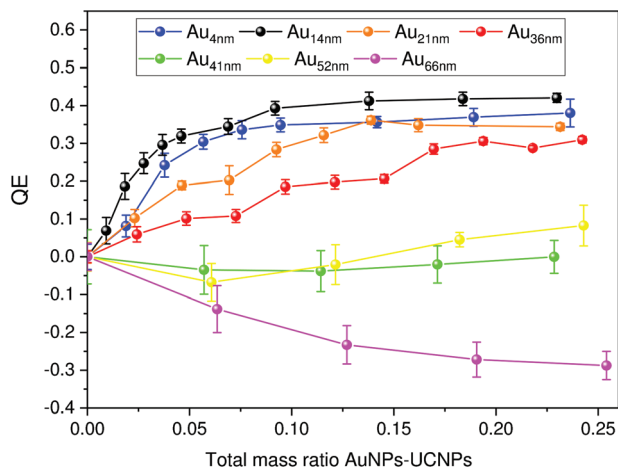


Fig. 5 Upconversion luminescence quenching efficiency, QE (from eqn (1)), as a function of the total mass of AuNPs normalized to the total mass of UCNPs. Different curves correspond to different AuNP sizes.

luminescence quenching to luminescence enhancement. Furthermore, a maximum quenching efficiency is achieved for an optimum AuNP size, above which the QE decreases (see Fig. 5). Indeed, there is an intermediate range of AuNP sizes where both plasmon-induced phenomena roughly compensate each other to lead almost zero quenching (Au_{41 nm} – Au_{52 nm}). When the AuNP size used in the experiments exceeds this critical range, the enhancement phenomenon clearly dominates leading to negative values of QE.

3.1. Theoretical interpretation

For an accurate theoretical interpretation of the experimental findings, we performed a combined study of the emission of an UCNP interacting with an AuNP at a wavelength that matches the localized surface plasmon resonance of the latter. As a starting point, we study the decay of a single emitter near a gold nanoparticle using two strategies: the classical phenomenological model proposed by Gersten and Nitzan, which leads to analytical expressions,⁴³ and the finite-difference time-domain (FDTD) method (FDTD-Solutions software, Lumerical Inc.).⁴⁴ The first model describes the emission of a classical point dipole in proximity to an AuNP, by means of the gold macroscopic electromagnetic dielectric response. In particular, its radiative decay is obtained through the power radiated by the electric dipole moment of the system, whereas the non-radiative decay is calculated by means of the Joule heating power in the AuNP. By contrast, the FDTD method is based on the numerical integration of the full vectorial Maxwell equations in the system, and therefore, no truncated multipole expansion for the field is needed. These simulations are more demanding in terms of computational resources but they allow us to validate the results obtained using the previously approximated phenomenological model. Calculation of the decay rates is performed in a similar way to that in the Gersten and Nitzan's model, *i.e.*, by registering the total and the radiated power emitted by a classical dipole outside the

system. In all simulations we use a mesh size small enough to discretize the AuNP-diameter with at least 20 pixels (simulations with higher resolutions were checked to validate the mesh size).

In our model we consider an emitter at a distance d from the surface of a spherical AuNP with radius a , whose dielectric function ϵ is obtained from previously reported experimental data.⁴⁵ Then, we compute the radiative and non-radiative decay rates, normalized to the original radiative decay rate (in the absence of the AuNP) Γ_{R}^0 , for two different emitter dipole configurations: emitter dipole parallel ($\Gamma_{\text{R}}^{\parallel}$, $\Gamma_{\text{NR}}^{\parallel}$) or perpendicular ($\Gamma_{\text{R}}^{\perp}$, $\Gamma_{\text{NR}}^{\perp}$) to the AuNP surface. The resulting decays can be expressed as follows:

$$\frac{\Gamma_{\text{R}}^{\perp}}{\Gamma_{\text{R}}^0} = \left| 1 + 2 \left(\frac{a}{a+d} \right)^3 \frac{\epsilon - 1}{\epsilon + 2} \right|^2, \quad (2)$$

$$\frac{\Gamma_{\text{R}}^{\parallel}}{\Gamma_{\text{R}}^0} = \left| 1 - \left(\frac{a}{a+d} \right)^3 \frac{\epsilon - 1}{\epsilon + 2} \right|^2, \quad (3)$$

$$\frac{\Gamma_{\text{NR}}^{\perp}}{\Gamma_{\text{R}}^0} = \frac{-3c^3}{2\omega^3 a^3} \sum_i \frac{(2i+1)(i+1)^2 a^{2i+4}}{i(a+d)^{2i+4}} \text{Im} \left\{ \frac{1}{\epsilon + \frac{i+1}{i}} \right\}, \quad (4)$$

$$\frac{\Gamma_{\text{NR}}^{\parallel}}{\Gamma_{\text{R}}^0} = \frac{-3c^3}{4\omega^3 a^3} \sum_i \frac{(2i+1)(i+1) a^{2i+4}}{(a+d)^{2i+4}} \text{Im} \left\{ \frac{1}{\epsilon + \frac{i+1}{i}} \right\}, \quad (5)$$

where c is the speed of light and ω is the green luminescence frequency under consideration. Last, we average both emitter configurations (parallel and perpendicular to the AuNP surface) to obtain the total radiative Γ_{R} and non-radiative Γ_{NR} decay rates. Fig. 6 presents the simulated decay rates for the two representative AuNP sizes according to our experiments: Au_{21 nm} for luminescence quenching and Au_{66 nm} for luminescence enhancement.

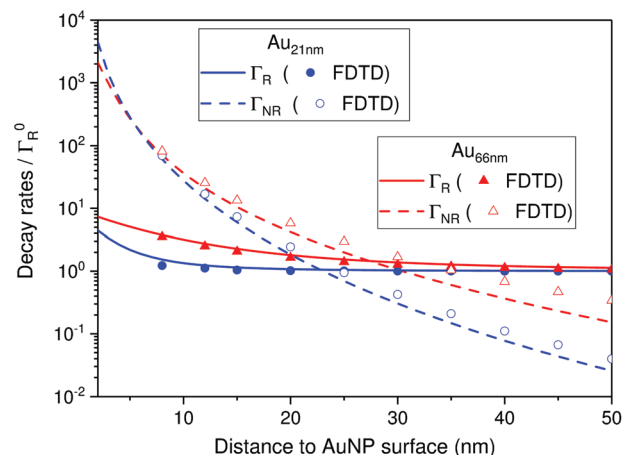


Fig. 6 Simulated radiative Γ_{R} (solid line) and non-radiative Γ_{NR} (dashed line) decay rates of an emitter as a function of its distance to the AuNP surface for two AuNP sizes: Au_{21 nm} (blue) and Au_{66 nm} (red). Symbols correspond to the decay rates obtained through FDTD simulations. The emission wavelength under consideration is 540 nm.

science enhancement. Note that the size of the AuNP significantly affects the behavior of the decay rates as a function of the distance to the emitter. Indeed, our results suggest that large AuNPs can affect emitters at a larger distance from their surfaces than the small AuNPs. More interestingly, for large AuNPs a significant increase of the radiative decay rate takes place, and therefore a relevant Purcell effect competes with RET. In Fig. 6 we also plot the radiative Γ_R and non-radiative Γ_{NR} decay rates calculated through the FDTD simulations (symbols), which reproduce the behavior obtained within the analytical classical model.

As we show in Fig. 6, the decay rates of a single emitter strongly depend on the distance of the emitters to the AuNP surface. Therefore, in order to theoretically calculate the quenching efficiency of the UCNP, we consider a random uniform distribution of multiple emitters (Er^{3+} ions) inside the UCNP interacting with the AuNP.⁴⁶ The quenching efficiency of a single emitter is evaluated by considering its emission enhancement (or quenching) I/I_0 related to the change of its quantum yield as follows:^{47,48}

$$\text{QE}_{\text{Er}} = 1 - \frac{I}{I_0}, \quad (6)$$

$$\frac{I}{I_0} = \frac{\eta}{\eta_0} = \frac{\Gamma_R/I_R^0}{(\Gamma_R/I_R^0 + \Gamma_{NR}/I_R^0)\eta_0 + 1 - \eta_0},$$

where η (η_0) represents the intrinsic quantum yields of the emitter in the presence (absence) of the AuNP. Note that η (η_0) measures the probability of a single excited Er^{3+} ion to be de-excited radiatively in the presence (absence) of the AuNP. As previously discussed, the excitation enhancement in eqn (6) is considered negligible.

By evaluating eqn (6), we first compute the quenching efficiency for every single Er^{3+} ion, QE_{Er} , which implicitly depends on its distance to the AuNP surface by way of the corresponding decay rates. Afterwards, the quenching efficiency of the UCNP was calculated by averaging the efficiency of each Er^{3+} ion inside the UCNP: $\text{QE} = \langle \text{QE}_{\text{Er}} \rangle_{N_{\text{Er}}}$. In our simulations the number of Er^{3+} ions inside the upconverting nanoparticle is $N_{\text{Er}} = f_{\text{Er}} m N_A / W \approx 715$, where $f_{\text{Er}} = 0.019$ is the fraction of Er^{3+} ions, $W = 205.3 \text{ g mol}^{-1}$ is the molar weight of $\text{NaYF}_4:\text{Yb/Er}$, and $m = 1.28 \times 10^{-17} \text{ g}$ is the mass of the UCNP (with no silica shell).

Fig. 7 shows the simulated QE as a function of the AuNP diameter for different values of the intrinsic quantum yield η_0 (solid lines). A rough estimation of the intrinsic quantum yield of $\eta_0 \approx 0.08$ results from considering a typical radiative lifetime for the excited-green level ($^4\text{S}_{3/2}$) in the millisecond range, and its measured luminescence lifetime which is $\sim 80 \mu\text{s}$ (shown later). It is worth noting that this value agrees with previous considerations by Bhuckory *et al.* based on FRET measurements of UCNPs with different core/shell architectures where values of η_0 between 1% and 30% were estimated.⁴⁹ Here, we consider values of η_0 close to the value estimated from our lifetime measurements and within the reported range. In all cases, the general trend of the luminescence quenching

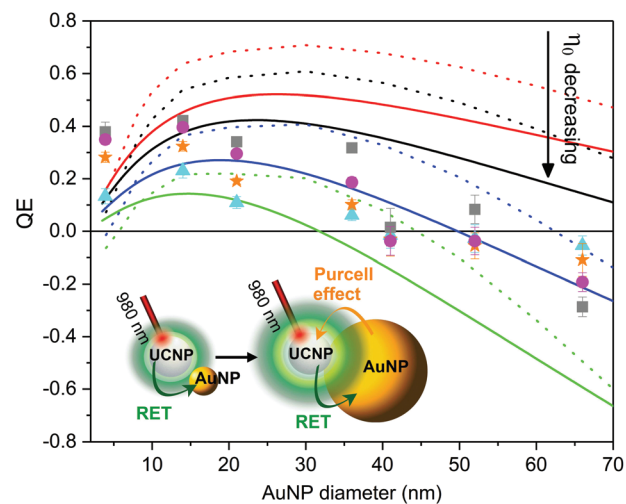


Fig. 7 Simulated (lines) and experimental (symbols) upconversion luminescence quenching efficiency versus the AuNP diameter. Simulated QE curves for different values of η_0 : 0.15 (red line), 0.1 (black line), 0.05 (blue line) and 0.025 (green line). Solid lines were obtained through the Gersten and Nitzan model after averaging the contribution of all the Er^{3+} ions inside the UCNP. Dotted lines were obtained by means of FDTD simulations using a single emitter (ion) at a fixed distance from the AuNP surface (12 nm). Experimental QE data for different mass ratios of AuNPs–UCNPs: 0.025 (triangle), 0.05 (star), 0.1 (circle) and 0.25 (square).

efficiency is as follows: the QE initially increases and, after reaching a maximum value, it decreases with the increase of the AuNP size. Therefore, there is an optimum AuNP size to reach the maximum quenching, which agrees with the experimental findings. This is a crucial result regarding the design of an optimum UCNP–AuNP pair to develop RET-based applications. Another interesting feature is the transition from luminescence quenching to enhancement as the AuNP diameter increases. The occurrence of such a transition depends on the value of the intrinsic quantum yield η_0 . In fact, for the lowest values of η_0 used in Fig. 7, the luminescence enhancement is achieved for AuNP sizes of the order of those used in the experiments. For comparison purposes, symbols shown in Fig. 7 indicate the experimental values of QE for a fixed mass ratio between the AuNPs and the UCNPs (see Fig. 5). Remarkably, very good agreement between experiments and simulations takes place. To reinforce our theoretical results, we have also developed simulations using FDTD, although in this case we used a single Er^{3+} ion placed at a distance of 12 nm from the AuNP surface (corresponding to roughly the center of the UCNP). The FDTD-simulated QE curves are also plotted in Fig. 7 (dashed lines) for different values of η_0 . These FDTD results corroborate the main general trends found with the phenomenological model: the existence of an optimum AuNP size for maximum quenching, and a transition between quenching and enhancement with the gold particle diameter. Still, its quantitative agreement is not perfect due to the averaging process carried out with the classical model. Indeed, this discrepancy reveals the relevance of analyzing the problem

as a multiple emitter system interacting with the AuNP. It is to be noticed that there could be other intrinsic deviations due to the approximations of the model as well.

For further analysis of this phenomenon, Fig. 8 shows the distribution of Er^{3+} ions (points) inside an 18 nm UCNP with a silica shell of 3.8 nm, as in the experiments, in contact to a AuNP placed at the north pole of the UCNP. The enhancement factor of every Er^{3+} ion, $(\eta/\eta_0)_{\text{Er}}$, is represented by its color specified by the color bar shown in the figure. Results for a 21 nm-diameter AuNP (left panel) and for a 66 nm-diameter AuNP (right panel) are plotted. For $\text{Au}_{21\text{ nm}}$ we observe that the ions placed at the north hemisphere exhibit a strong quenching whereas the rest of the ions do not experience any effect. However, for $\text{Au}_{66\text{ nm}}$ most of the ions show enhancement and only a few ions very close to the north pole exhibit quenching. This is also indicated in the lower panel of Fig. 8 where the distribution of the quenching efficiency for each Er^{3+} ion is plotted as a function of its distance to the AuNP surface for both AuNP sizes. These results, after averaging, are consistent with the trends shown in Fig. 7.

According to this interpretation, larger UCNPs are expected to show a smaller net quenching or enhancement efficiency. Note that the luminescence contributed by the different ions inside the UCNP depends on their distance to the AuNP surface. Thus, the ions in larger UCNPs are expected to contribute within a larger QE range, *i.e.*, a smaller proportion of ions within the nanoparticle experience strong enhancement or quenching. The resulting averaged effect will reduce the final values of QE accordingly. To address this issue we measured the QE of a mixture of 100 μL of an ethanol dispersion of 34 nm-diameter UCNPs covered with a 4.4 nm silica shell at 0.1 g L^{-1} with an increasing volume of AuNP aqueous dispersions. We considered AuNP sizes chosen as those providing maximum quenching ($\text{Au}_{14\text{ nm}}$) and maximum enhance-

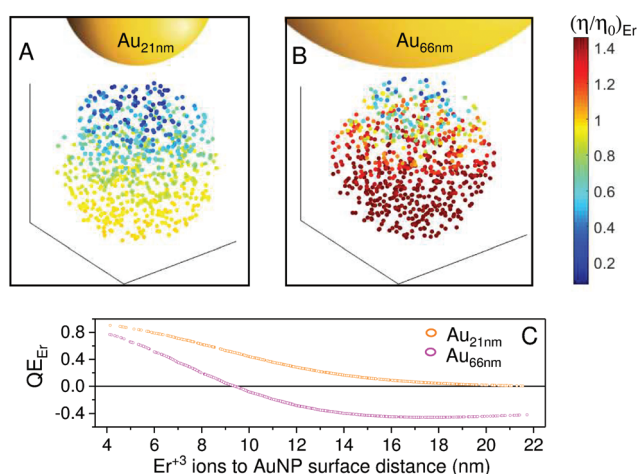


Fig. 8 (A–B) Simulated distribution of the enhancement factor of each individual Er^{3+} ion $(\eta/\eta_0)_{\text{Er}}$ for a AuNP with 21 nm diameter (panel A) or with 66 nm diameter (panel B) placed at the north pole of the UCNP. (C) Simulated quenching efficiency for each Er^{3+} ion, QE_{Er} , as a function of its distance to the AuNP surface for both AuNPs: $\text{Au}_{21\text{ nm}}$ and $\text{Au}_{66\text{ nm}}$.

ment ($\text{Au}_{66\text{ nm}}$); see Fig. 5. Results plotted in Fig. S4† show a significant reduction of the quenching and enhancement effects, as expected from our theoretical interpretation regarding the effect of the AuNP size on larger UCNPs.

3.2. Luminescence lifetime analysis

So far, we have established that intensity quenching or enhancement of the green luminescence of UCNPs is due to the interplay between two plasmon-induced effects: luminescence non-radiative RET and enhancement of the radiative decay rate (Purcell effect). Since both phenomena affect the total decay rate of the excited green levels $^2\text{H}_{11/2}$ and $^4\text{S}_{3/2}$ (see Fig. 1B), the green luminescence lifetime is expected to change due to the AuNP proximity. Thus, luminescence decay signals for Er^{3+} ions at 540 nm ($^2\text{H}_{11/2}, ^4\text{S}_{3/2} \rightarrow ^4\text{I}_{15/2}$) were measured for an additional validation of our study. In Fig. 9A and B we plot the luminescence decay signals for the APTES-UCNP and non-APTES-UCNP ethanol dispersions before (left panels) and after (right panels) adding 8 μL of the AuNP aqueous dispersion. Results for the two cases used so far as representative of luminescence quenching, $\text{Au}_{21\text{ nm}}$ (Fig. 9A), and luminescence enhancement, $\text{Au}_{66\text{ nm}}$ (Fig. 9B), are shown.

In all cases luminescence signals show an initial increase and a signature of the ETU mechanism exciting Er^{3+} ions from excited Yb^{3+} ions within the UCNPs, followed by a roughly exponential decay. As expected, the upconversion luminescence of APTES-UCNP and non-APTES-UCNP samples leads to the same decay rate in the absence of AuNPs (Fig. 9A and B, left panel). However, in the APTES-UCNP sample the interaction between the AuNPs and the UCNPs mediated by APTES leads to a slightly faster decay in comparison with the non-APTES-UCNP sample. In particular, this effect reduces the luminescence lifetime from $\tau_{\text{NA}} = 81.3 \pm 0.8 \mu\text{s}$ ($83 \pm 1 \mu\text{s}$) to τ_{A}

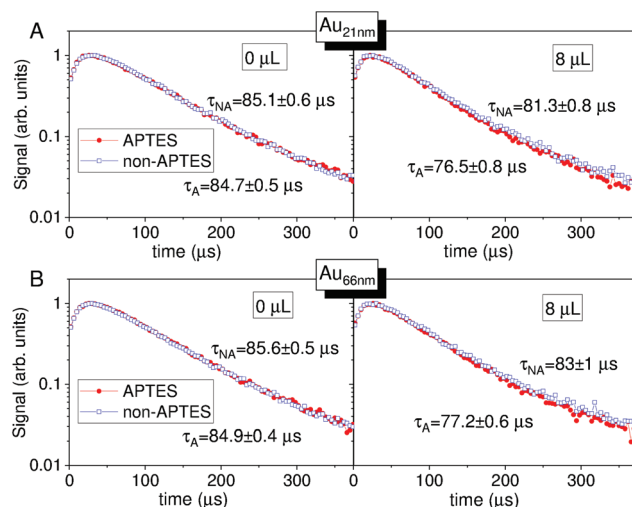


Fig. 9 Normalized luminescence decay curves at 540 nm in a semilog scale for APTES-UCNP (solid red circles) and non-APTES-UCNP (open blue squares) dispersions with $\text{Au}_{21\text{ nm}}$ (A), and $\text{Au}_{66\text{ nm}}$ (B). The left (right) panel corresponds to 100 μL of 0.1 g L^{-1} UCNP ethanol dispersion before (after) adding 8 μL of the AuNP aqueous dispersion.

= 76.5 ± 0.8 μs (77.2 ± 0.6 μs). The relative change in the luminescence lifetime due to the interaction with the AuNPs of both sizes is $1 - \tau_A/\tau_{NA} \simeq 6-7\%$. Thus, this reduction is a clear confirmation of the occurrence of a plasmon-induced modification of the upconversion luminescence of the UCNPs.

Let us theoretically interpret the latter experimental results by keeping in mind that a modification of the total decay rate of the excited green level (${}^2\text{H}_{11/2}$ and ${}^4\text{S}_{3/2}$) is not directly reproduced in the upconversion luminescence lifetime. In contrast, the upconversion luminescence dynamics is a complex process involving many more mechanisms than the radiative and non-radiative decay rates from the green level, such as for example the energy transfer from Yb^{3+} ions to Er^{3+} ions, or other decay rates from intermediate energy levels. Therefore, in order to account for the upconversion luminescence dynamics we use the following rate equations which describe the main physical mechanisms (see Fig. S5† for further details):

$$\begin{aligned} \frac{dN_1}{dt} &= -\Gamma_1 N_1 + \Gamma_{21} N_2 - K_3 N_1 N_1^Y, \\ \frac{dN_2}{dt} &= -\Gamma_2 N_2 + \Gamma_{32} N_3 + K_2 N_0 N_1^Y - K_{B2} N_2 N_0^Y - K_4 N_2 N_1^Y, \\ \frac{dN_3}{dt} &= -\Gamma_3 N_3 + \Gamma_{43} N_4 + K_3 N_1 N_1^Y, \\ \frac{dN_4}{dt} &= -\Gamma_4 N_4 + K_4 N_2 N_1^Y, \\ \frac{dN_1^Y}{dt} &= -\Gamma_1^Y N_1^Y + \frac{\Gamma_1^Y I}{2I_{\text{sat}}} (N_0^Y - N_1^Y) - K_2 N_0 N_1^Y + K_{B2} N_2 N_0^Y \\ &\quad - K_3 N_1 N_1^Y - K_4 N_2 N_1^Y. \end{aligned} \quad (7)$$

Here N_j is the density of Er^{3+} ions in the energy level j , where the subscripts $j = 0, 1, 2, 3$, and 4 represent the ${}^4\text{I}_{15/2}$, ${}^4\text{I}_{13/2}$, ${}^4\text{I}_{11/2}$, ${}^4\text{F}_{9/2}$, and ${}^4\text{S}_{3/2}$ energy levels of Er^{3+} ions, respectively. Fast-decaying levels such as ${}^4\text{F}_{7/2}$ and ${}^4\text{I}_{9/2}$ were not taken into account. The energy level ${}^2\text{H}_{11/2}$ usually is considered as a single level together with the ${}^4\text{S}_{3/2}$ level since they are very close in energy. N_0^Y and N_1^Y are the densities of Yb^{3+} ions in the energy levels ${}^2\text{F}_{7/2}$ and ${}^2\text{F}_{5/2}$, respectively. Γ_{jl} is the decay rate from level j to level l whereas Γ_j (Γ_j^Y for Yb^{3+} ions) is the total decay rate of the energy level j . On the other hand K_2 , K_3 and K_4 are the coefficients of the RET from the Yb^{3+} ion (donor) to the levels 2, 3, and 4 of the Er^{3+} ion (acceptor), respectively. K_{B2} is the coefficient of back energy transfer from the Er^{3+} ion in level 2 to the Yb^{3+} ion. The interaction of the Er^{3+} ions with the AuNP is introduced by means of an additional decay rate Γ_{40}^{Au} from the green level 4 to the ground level 0. This additional decay is expected to be much larger than Γ_{40} in order to account for both the non-radiative energy transfer to the AuNP and the increase of the radiative decay rate due to the Purcell effect.

In our simulations, we consider decays and RET coefficients of the order of those found in the literature (see section S5 in the ESI† for details). In addition, we used a value for the intrinsic quantum yield associated with the green emitting level $\eta_0 = \Gamma_{40}/\Gamma_4 \sim 0.04$ in agreement with the one in Fig. 7. This value is chosen so that N_4 population decay matches the experimental luminescence lifetime ($\simeq 85 \mu\text{s}$). Within these considerations,

we solved eqn (7) using an explicit Runge-Kutta method in MatLab.⁵⁰ First, we analyze the time evolution of the population N_4 for a value of the decay rate of $\Gamma_{40}^{\text{Au}} = 15\Gamma_{40}$. This value is roughly estimated from the decay rate curves shown in Fig. 6 for an Er^{3+} ion placed at a distance to the AuNP surface of 12 nm (close to the UCNP center). In Fig. 10A we plot the time evolution of the population N_4 when the system is excited with a pulse laser of 40 μs which is exponentially fitted such as the experimental data. Such numerical analysis is performed in the absence and in the presence of the additional decay associated with the AuNP, and the obtained decay time results are $\tau_0 = 86 \mu\text{s}$ and $\tau = 80.5 \mu\text{s}$, respectively (see Fig. 10A). Thus, our simulations reproduce a relative change of the ${}^4\text{S}_{3/2}$ level population lifetime of $1 - \tau/\tau_0 \simeq 0.064$, which agrees with the experimental results. Note that the change in the green emitting level population lifetime, induced by the AuNP, is only of $\sim 6\%$, despite the fact that the modification induced in its total decay rate Γ_4 is $1 - \Gamma_4/(\Gamma_4 + \Gamma_{40}^{\text{Au}}) \sim 38\%$.

As a final analysis, we study the global behavior of the UCNP in proximity to the AuNP by taking into account the population N_4 decay curve for all the Er^{3+} ions inside the UCNP. Therefore, we consider a different Γ_{40}^{Au} for every Er^{3+} ion, according to its distance to the AuNP surface. The green emitting level population lifetime is then evaluated by averaging the population lifetime obtained for each ion $\langle \tau_{\text{Er}} \rangle_{N_{\text{Er}}}$. In order to have an idea of the effect induced in every Er^{3+} ion inside the UCNP, Fig. 10B shows the distribution of the ratio of the ${}^4\text{S}_{3/2}$ lifetime in both the presence and absence of a Au_{21} nm NP placed at the UCNP north pole, $(\tau/\tau_0)_{\text{Er}}$. As shown, the ions placed at the north hemisphere are the most influenced by the Au_{21} nm NP and, therefore, their decay becomes faster (from 10% to 5% of the relative change). In contrast, the effect on ions at the south hemisphere is negligible. By averaging the lifetime of all ions inside the UCNP, our calculations give rise to a relative change in the lifetime of 5% (7%) in the case of Au_{21} nm (Au_{66} nm) NPs. Both values are in perfect agreement with those experimentally found for the luminescence lifetime.

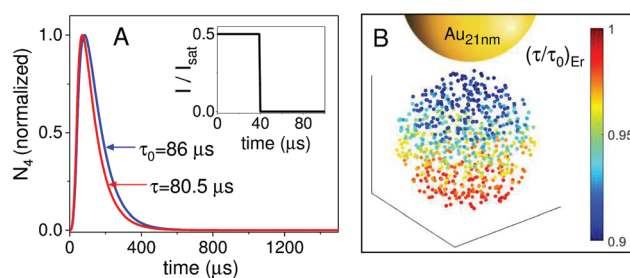


Fig. 10 (A) Simulated normalized decay curve of the population N_4 of energy level ${}^4\text{S}_{3/2}$ in the absence (blue line) and in the presence (red line) of an AuNP. An additional decay rate of $\Gamma_{40}^{\text{Au}} = 15\Gamma_{40}$ accounts for the effect of the AuNP in the model. (B) Simulated distribution of the ratio of the N_4 population lifetime in the presence and absence of a Au_{21} nm NP for every Er^{3+} ion inside the UCNP, $(\tau/\tau_0)_{\text{Er}}$. The AuNP is placed at the north pole of the UCNP and its effect on every ion is simulated with a distance-dependent Γ_{40}^{Au} .

3.3. Optimization of quenching/enhancement performance: the role of the SiO₂ shell thickness and UCNP size

Finally, let us use our theoretical model to discuss a general guideline for optimum design of UCNP–AuNP hybrid systems. We study the quenching/enhancement efficiency as we change both the UCNP size and the SiO₂ shell thickness covering the UCNP. First, we analyze the effect of the silica shell by considering UCNPs with the same size as the one used in the experiments (18 nm of diameter) but with a tunable SiO₂ shell thickness. For the sake of simplicity, we assume that the intrinsic quantum yield η_0 does not significantly change with the SiO₂ thickness for shells beyond a few nanometers and, therefore, we consider the same value $\eta_0 = 0.06$ for all cases. Fig. 11A shows a contour plot of the quenching efficiency as a function of the AuNP size and the SiO₂ shell thickness. There, we observe that thinner shells provide larger quenching as expected since RET will be stronger when reducing the distance between the Er³⁺ ions and the AuNP surface. Therefore, a UCNP will theoretically achieve the best quenching performance without a SiO₂ shell. Experimentally, however, no SiO₂ shell will be impractical because a shell is needed to attach functional groups and to shield the outermost luminescent ions from solvent interactions. The optimum quenching is achieved for AuNPs of size around 20 nm. On the other hand, luminescence enhancement occurs for large AuNPs. This enhancement increases with the SiO₂ thickness since in that case most of the Er³⁺ ions are too far to suffer strong quenching and, in contrast, they exhibit enhancement. Fig. 11A shows that the optimal scenario for enhancing luminescence results from a SiO₂ thickness of around ~12 nm.

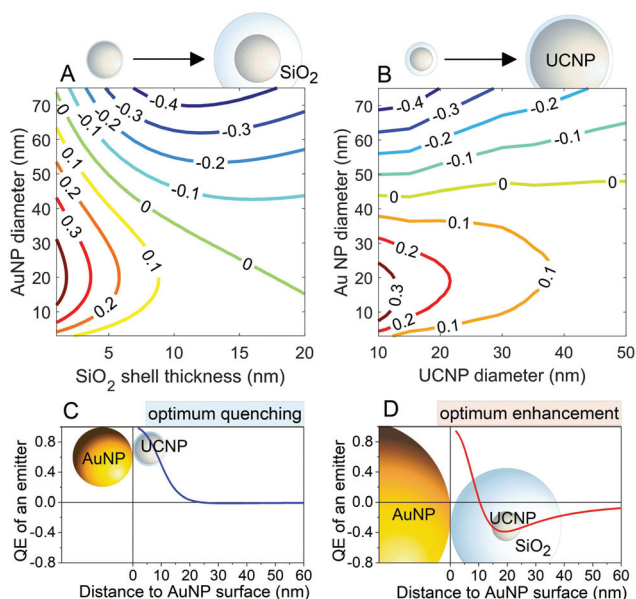


Fig. 11 Contour plot of the simulated upconversion luminescence quenching efficiency as a function of the AuNP diameter and (A) the SiO₂ shell thickness of a UCNP with a diameter of 18 nm; and (B) the diameter of a UCNP with a SiO₂ shell thickness of 3.8 nm. Schematic view of optimum (C) quenching and (D) enhancement performance.

Last, let us analyze the role of the UCNP size in the quenching/enhancement performance. In our simulations we vary the size of the UCNP, while keeping the SiO₂ shell thickness constant and equal to the experimental value of 3.8 nm. However, the quantum yield of UCNPs is expected to change with the particle size. In fact, the green luminescence decay rate of UCNPs Γ_4 has been found to increase linearly with their surface area to volume ratio.^{51–53} Thus, we use the linear fit obtained by Lim *et al.*⁵¹ (see their Fig. 3) to compute Γ_4 and estimate the intrinsic quantum yield values $\eta_0 = \Gamma_{40}/\Gamma_4$. Here, a radiative decay time of $1/\Gamma_{40} \approx 1$ ms was considered. Fig. 11B shows a contour plot of the quenching efficiency as a function of AuNP and UCNP diameters. There, it is demonstrated that a stronger change in luminescence will arise in smaller UCNPs. In particular, the optimum quenching is achieved for the UCNP with the smallest size and for AuNPs with a diameter of around 15 nm. Again, luminescence enhancement occurs for large AuNPs. Small UCNPs exhibit optimum enhancement since increasing the UCNP size will affect ions inside the UCNP differently (as shown before), resulting in a decrease of the overall enhancement.

As a summary, an optimum quenching-based biosensor will use small UCNPs capped with a thinner silica shell to favor the proximity of all the Er³⁺ ions to the AuNP surface, and AuNPs big enough to produce a significant effect at long distances but not too large to produce luminescence enhancement, that is, between 15 and 20 nm. We show a schematic view of this optimum system in Fig. 11C where we plot the quenching efficiency of an emitter as a function of the distance from the surface of a 20 nm-gold nanoparticle. Moreover, the design of a hybrid-system based on luminescence enhancement will require larger AuNPs, with diameters above 50 nm. These AuNPs will produce quenching at short distances from their surface, and luminescence enhancement at intermediate distances. Thus, the ideal system will be such that all ions inside the UCNP belong to the maximum enhancement region. Therefore, small UCNPs capped with a silica shell which avoids the quenching region will result in optimum performance. Fig. 11D shows a schematic view of this optimum enhancement system for a gold nanoparticle of 65 nm diameter.

4. Conclusions

A careful selection of UCNP–AuNP pairs is crucial for achieving optimal results in resonant energy transfer nanosystems for sensing and biosensing applications. This study highlights the role of the relative sizes of nanoparticles in the plasmon-assisted upconversion luminescence of NaYF₄:Yb,Er@SiO₂ UCNPs. We employed AuNPs with diameters ranging from 4 nm to 66 nm, well below and above the UCNP size in our experiments, which was 18 nm. AuNPs were adsorbed on the UCNP surface *via* amine groups on the UCNP 3.8 nm thick silica shell. We found a continuous transition from quenching to luminescence enhancement due to the AuNP size. Due to competing plasmonic effects, increasing the AuNP size leads

to a reduced quenching efficiency until reaching the opposite effect, *i.e.* luminescence enhancement. Furthermore, UCNP–AuNP coupling leads to a reduction of the upconversion luminescence lifetime, indicative of an increase of the total decay rate for the excited UCNPs.

We found a AuNP–UCNP pair with diameters ~14 nm and 18 nm, respectively, to be optimal for a luminescence quenching detection strategy, since it provides the largest detection dynamic range stretching from 0% to 40% quenching. On the other hand, the luminescence enhancement observed with 66 nm AuNPs, as well as the room for improvement by using larger AuNPs and better tuning the UCNP/AuNP distance, suggests the potential of sensors based on luminescence enhancement as an alternative strategy.

Our experimental findings were theoretically reproduced using a classical phenomenological model and a direct integration of the full vectorial Maxwell equations. Both approaches show a competition between RET and the Purcell effect as the AuNP size increases, which eventually leads to luminescence enhancement for large enough AuNP diameters. Our theoretical analysis reveals that small values of the UCNP intrinsic quantum yield favor the appearance of the quenching-to-enhancement transition for smaller AuNP sizes. Moreover, we pinpoint the role of Er^{3+} ion spatial distribution in the UCNPs. By averaging the contribution of each of the ions to the quenching or enhancement efficiency, we quantified the total effect in very good agreement with the experimental evidence.

Finally, a complete general analysis of the optimization of the hybrid system for maximum quenching or enhancement was carried out in the framework of the developed theoretical model. Gold nanoparticles with diameters of 15–20 nm and small UCNPs with very thin SiO_2 shells are found to provide the best results if biosensing based on luminescence quenching is pursued. On the other hand, a biosensor based on luminescence enhancement would need AuNPs bigger than 50 nm, combined with small UCNPs and SiO_2 shells slightly above 10 nm.

Conflicts of interest

There are no conflicts to declare.

Acknowledgements

This work was supported by UCM-Santander (PR26/16-12B), Ministerio de Economía y Competitividad (MAT2016-75955, MAT2017-83111R, and FIS2017-87360-P), Ministerio de Ciencia, Innovación y Universidades (RTI2018-094859-B-I00), and Comunidad de Madrid (B2017/BMD-3867 RENIM-CM) co-financed by European Structural and Investment Fund. D. M. G. thanks UCM-Santander for a pre-doctoral contract (CT17/17-CT18/17). We thank A. Villas for his collaboration at an early stage of the work. TEM images were obtained at the

National Center for Electron Microscopy (UCM, Madrid) facility.

References

- 1 H. Dong, S.-R. Du, X.-Y. Zheng, G.-M. Lyu, L.-D. Sun, L.-D. Li, P.-Z. Zhang, C. Zhang and C.-H. Yan, *Chem. Rev.*, 2015, **115**, 10725–10815.
- 2 S. Wilhelm, *ACS Nano*, 2017, **11**, 10644–10653.
- 3 S. Wen, J. Zhou, K. Zheng, A. Bednarkiewicz, X. Liu and D. Jin, *Nat. Commun.*, 2018, **9**, 2415.
- 4 X. Qin, J. Xu, Y. Wu and X. Liu, *ACS Cent. Sci.*, 2019, **5**, 29–42.
- 5 F. Auzel, *Chem. Rev.*, 2004, **104**, 139–173.
- 6 A. W. Kueny, W. E. Case and M. E. Koch, *J. Opt. Soc. Am. B*, 1993, **10**, 1834–1839.
- 7 F. Wang, R. Deng, J. Wang, Q. Wang, Y. Han, H. Zhu, X. Chen and X. Liu, *Nat. Mater.*, 2011, **10**, 968.
- 8 D. R. Gamelin and H. U. Güdel, *Acc. Chem. Res.*, 2000, **33**, 235–242.
- 9 D. Mendez-Gonzalez, E. Lopez-Cabarcos, J. Rubio-Retama and M. Laurenti, *Adv. Colloid Interface Sci.*, 2017, **249**, 66–87.
- 10 Z. Zhang, S. Shikha, J. Liu, J. Zhang, Q. Mei and Y. Zhang, *Anal. Chem.*, 2019, **91**, 548–568.
- 11 N. Hildebrandt, C. M. Spillmann, W. R. Algar, T. Pons, M. H. Stewart, E. Oh, K. Susumu, S. A. Díaz, J. B. Delehanty and I. L. Medintz, *Chem. Rev.*, 2016, **117**, 536–711.
- 12 Y. Han, M. O. Noor, A. Sedighi, U. Uddayasankar, S. Doughan and U. J. Krull, *Langmuir*, 2017, **33**, 12839–12858.
- 13 S. Melle, O. G. Calderón, M. Laurenti, D. Mendez-Gonzalez, A. Egatz-Gómez, E. López-Cabarcos, E. Cabrera-Granado, E. Díaz and J. Rubio-Retama, *J. Phys. Chem. C*, 2018, **122**, 18751–18758.
- 14 D. M. Wu, A. García-Etxarri, A. Salles and J. A. Dionne, *J. Phys. Chem. Lett.*, 2014, **5**, 4020–4031.
- 15 D. Lu, S. K. Cho, S. Ahn, L. Brun, C. J. Summers and W. Park, *ACS Nano*, 2014, **8**, 7780–7792.
- 16 Q.-C. Sun, H. Mundoor, J. C. Ribot, V. Singh, I. I. Smalyukh and P. Nagpal, *Nano Lett.*, 2014, **14**, 101–106.
- 17 M. Saboktakin, X. Ye, U. K. Chettiar, N. Engheta, C. B. Murray and C. R. Kagan, *ACS Nano*, 2013, **7**, 7186–7192.
- 18 W. Zhang, F. Ding and S. Y. Chou, *Adv. Mater.*, 2012, **24**, OP236–OP241.
- 19 A. Das, S. Mao, C. Cho, K. Kim and W. Park, *Nat. Commun.*, 2018, **9**, 4828.
- 20 N. J. Greybush, M. Saboktakin, X. Ye, C. Della Giovampaola, S. J. Oh, N. E. Berry, N. Engheta, C. B. Murray and C. R. Kagan, *ACS Nano*, 2014, **8**, 9482–9491.
- 21 G. Yi, B.-S. Moon, X. Wen, Y.-J. Kim and D.-H. Kim, *J. Phys. Chem. C*, 2018, **122**, 13047–13053.

- 22 A. L. Feng, M. L. You, L. Tian, S. Singamaneni, M. Liu, Z. Duan, T. J. Lu, F. Xu and M. Lin, *Sci. Rep.*, 2015, **5**, 7779.
- 23 K. A. Kang, J. Wang, J. B. Jasinski and S. Achilefu, *J. Nanobiotechnol.*, 2011, **9**, 16.
- 24 F. Zhang, G. B. Braun, Y. Shi, Y. Zhang, X. Sun, N. O. Reich, D. Zhao and G. Stucky, *J. Am. Chem. Soc.*, 2010, **132**, 2850–2851.
- 25 M. Saboktakin, X. Ye, S. J. Oh, S.-H. Hong, A. T. Fafarman, U. K. Chettiar, N. Engheta, C. B. Murray and C. R. Kagan, *ACS Nano*, 2012, **6**, 8758–8766.
- 26 W. Ge, X. R. Zhang, M. Liu, Z. W. Lei, R. J. Knize and Y. Lu, *Theranostics*, 2013, **3**, 282–288.
- 27 S. Schietinger, T. Aichele, H.-Q. Wang, T. Nann and O. Benson, *Nano Lett.*, 2010, **10**, 134–138.
- 28 H. Zhang, Y. Li, I. Ivanov, Y. Qu, Y. Huang and X. Duan, *Angew. Chem., Int. Ed.*, 2010, **49**, 2865–2868.
- 29 S.-Z. Zhang, L.-D. Sun, H. Tian, Y. Liu, J.-F. Wang and C.-H. Yan, *Chem. Commun.*, 2009, **1**, 2547–2549.
- 30 Q. Wu, Q. Long, H. Li, Y. Zhang and S. Yao, *Talanta*, 2015, **136**, 47–53.
- 31 Z. Li, L. Wang, Z. Wang, X. Liu and Y. Xiong, *J. Phys. Chem. C*, 2011, **115**, 3291–3296.
- 32 S. Liu, G. Chen, T. Y. Ohulchanskyy, M. T. Swihart and P. N. Prasad, *Theranostics*, 2013, **3**, 275–281.
- 33 B. V. Enustun and J. Turkevich, *J. Am. Chem. Soc.*, 1963, **85**, 3317–3328.
- 34 N. G. Bastús, J. Comenge and V. Puntes, *Langmuir*, 2011, **27**, 11098–11105.
- 35 Z. Li and Y. Zhang, *Nanotechnology*, 2008, **19**, 345606.
- 36 P. Alonso-Cristobal, M. A. Lopez-Quintela, R. Contreras-Caceres, E. Lopez-Cabarcos, J. Rubio-Retama and M. Laurenti, *RSC Adv.*, 2016, **6**, 100614–100622.
- 37 R. L. McCally, *Appl. Opt.*, 1984, **23**, 2227–2227.
- 38 T. Stacewicz and M. Krainska-Miszczak, *Meas. Sci. Technol.*, 1997, **8**, 453–455.
- 39 M. Zhou, C. Zeng, Y. Chen, S. Z. Matthew, Y. Sfeir, M. Zhu and R. Jin, *Nat. Commun.*, 2016, **7**, 13240.
- 40 P. Mulvaney, *MRS Bull.*, 2001, **26**, 1009–1014.
- 41 M. A. El-Sayed, *Acc. Chem. Res.*, 2001, **34**, 257–264.
- 42 T. Hendel, M. Wuihschick, F. Kettemann, A. Birnbaum, K. Rademann and J. Polte, *Anal. Chem.*, 2014, **86**, 11115–11124.
- 43 J. Gersten and A. Nitzan, *J. Chem. Phys.*, 1981, **75**, 1139–1152.
- 44 A. T. Steven, G. Johnson and A. Oskooi, *Advances in FDTD Computational Electrodynamics: Photonics and Nanotechnology*, Artech House, Boston, USA, 2013.
- 45 P. B. Johnson and R. W. Christy, *Phys. Rev. B: Solid State*, 1972, **6**, 4370–4379.
- 46 D. E. Knuth, *The Art of Computer Programming, Vol 2: Seminumerical Algorithms*, Addison-Wesley, Boston, USA, 3rd edn, 1999.
- 47 R. Esteban, M. Laroche and J.-J. Greffet, *J. Appl. Phys.*, 2009, **105**, 033107.
- 48 X. Liu and D. Y. Lei, *Sci. Rep.*, 2015, **5**, 15235.
- 49 S. Bhuckory, E. Hemmer, Y.-T. Wu, A. Yahia-Ammar, F. Vetrone and N. Hildebrandt, *Eur. J. Inorg. Chem.*, 2017, 5186–5195.
- 50 J. R. Dormand and P. J. Prince, *J. Comput. Appl. Math.*, 1980, **6**, 19–26.
- 51 S. F. Lim, W. S. Ryu and R. H. Austin, *Opt. Express*, 2010, **18**, 2309–2316.
- 52 J. Zhao, Z. Lu, Y. Yin, C. McRae, J. A. Piper, J. M. Dawes, D. Jin and E. M. Goldys, *Nanoscale*, 2013, **5**, 944–952.
- 53 X. Xue, S. Uechi, R. N. Tiwari, Z. Duan, M. Liao, M. Yoshimura, T. Suzuki and Y. Ohishi, *Opt. Mater. Express*, 2013, **3**, 989–999.